Materials Research. 2025; 28(suppl. 1): e20250229
DOI: https://doi.org/10.1590/1980-5373-MR-2025-0229

FTIR and Raman Spectroscopic Characterization of Anionic Clays Obtained from Bauxite Tailings (Amazon, Brazil)

B.A.M. Figueira[a,b]* , J.A.S. Silva[c], R.S. Nascimento[d], G.R. Santos[b], A.G.A. Campos[b], M.L. Costa[d], P.T.C. Freire[e]

[a]*Universidade Federal do Pará, Programa de Pós-Graduação em Ciência e Engenharia de Materiais, Ananindeua, PA, Brasil.*
[b]*Universidade Federal do Pará, Faculdade de Química, Belém, PA, Brasil.*
[c]*Universidade Federal do Espírito Santo, Departamento de Física, Vitória, ES, Brasil.*
[d]*Universidade Federal do Pará, Programa de Pós-Graduação em Geologia e Geoquímica, Belém, PA, Brasil.*
[e]*Universidade Federal do Ceará, Departamento de Física, Fortaleza, CE, Brasil.*

Received: January 31, 2025; Revised: June 23, 2025; Accepted: July 03, 2025

Anionic clay-type materials with layered double hydroxide (LDH) structures in the MgAlFe and ZnAlFe ternary systems were successfully synthesized via co-precipitation, utilizing bauxite tailings from the Amazon region as the starting material. X-ray diffraction (XRD) confirmed the formation of well-defined LDH phases, with basal reflections indicative of the effective incorporation of divalent and trivalent cations into the lamellar structure. Scanning electron microscopy (SEM) revealed distinct morphological differences: MgAlFe LDHs exhibited rough, disordered surfaces, while ZnAlFe variants formed larger, plate-like aggregates. Raman and FTIR (ATR) spectroscopy identified characteristic vibrational bands, reflecting the influence of metallic composition on the structural organization of the materials. This study demonstrates a sustainable and efficient route for the synthesis of anionic clays from industrial waste, emphasizing their potential for technological and environmental applications.

Keywords: *Anionic clay, synthesis, bauxite tailings, spectroscopic characterization, Raman.*

1. Introduction

Anionic clays are inorganic compounds that belong to the layered double hydroxides (LDH) family, being among the scarcely clay minerals found on the earth's surface[1]. Their synthetic analogs are noted for their unique properties (anion exchange, thermal stability, acid-base nature, optical and conductivity properties), all of which are directly related to their chemical composition and lamellar structure[2,3]. Among the main practical applications of LDH-type materials are heterogeneous catalysis, supercapacitors, drug delivery hosts, adsorption of organic and inorganic pollutants and photocatalysis[2,4].

Chemically, anionic clays have general formula given as $[M_{1-x}^{2+}M_x^{3+}(OH)_2]^{x+}[A_{x/n}]^{n-}\cdot mH_2O$, where M^{2+} and M^{3+} denote di- and trivalent cations in the octahedral layer-type brucite, A^{n-} are the interlayer anions and *x* is the molar ratio $(M^{3+}/M^{2+}+M^{3+})$[1,3]. Although the structure can be formed from MOH_6 octahedral layers with di- and trivalent cations (binary system), the incorporation of a third cation (ternary system) or a tetravalent cation can also occur, which may result in a significant improvement in the previously mentioned technological applications[5-7].

In the conventional route, LDH-type materials are obtained from commercial reagents of divalent and trivalent metals, which are mixed in appropriate proportions in a solution under alkaline conditions, at low-temperatures, and for short-time hydrothermal conditions, that is, the co-precipitation method. However, there is currently an intense effort to synthesize these lamellar materials from natural sources and industrial waste, especially for economic and environmental reasons. For example, weathered tropical soils, dolomite source, bittern from seawater resource, eggshell bio-waste, municipal solid waste incineration fly ash, aluminum saline slags, electrode aluminum-foil industrial wastewater, phosphate tailings and red mud have been employed low-cost starting materials for the synthesis of anionic clays[8-16].

For upwards of two decades, the use of infrared and Raman spectroscopy has proven most useful for the detailed characterization of natural or synthetic anionic-type materials. For example, Kloprogge et al.[17] analyzed the IR and Raman spectrum of synthetic Mg/Zn/Al-hydrotalcites with different ratio atomics. They identified diagnostic bands for Zn-OH, Mg-OH, and Al-OH bonds, along with specific vibrational modes of anion-H_2O in the interlayer region, demonstrating these techniques as powerful tools for characterizing the chemical environments within these material structures. Frost and Erickson also conducted a similar characterization study using Raman spectroscopy of the desautelsite $(Mg_6Mn_2(CO_3)(OH)_{16}\cdot 4H_2O)$, indicating the technique's high effectiveness for both mineral characterization and identification of individual components (Mg-OH, Mn-OH and CO_3^{2-} vibrations)[18]. In addition, Frost, Weier and

*e-mail: figueiraufpa@gmail.com
Associate Editor: Eliana Muccillo.
Editor-in-Chief: Luiz Antonio Pessan.

Kloprogee have been successfully used Raman spectroscopy to investigate natural hydrotalcites with sulfate and carbonate anions in the interlayer region. They verified a reduction in the symmetry of both anionic species and concluded that the anions are bonded to the brucite-like hydroxyl surface and to the water in the interlayer[19]. Conversely, Frost et al.[20] synthesized hydrotalcites with phosphate anions into the interlayer space. The anionic species PO_4^{3-} and HPO_4^{2-} were detected by Raman spectroscopy at different pH ranges, indicating that their presence is pH-dependent during the synthesis process. These findings subsequently supported the application of hydrotalcites in environmental remediation processes, particularly for the uptake and immobilization of phosphates in contaminated environments.

The main objective of this work was to characterize layered-type materials with two different chemical compositions (MgAlFe and ZnAlFe) using vibrational spectroscopy (FTIR/ATR-Raman), SEM-EDS, and X-ray diffractometry (XRD). This multi-technique approach enabled a comprehensive understanding of the structural and morphological characteristics of MgAlFe and ZnAlFe anionic clays, providing insights into their potential for advanced material applications.

2. Materials and Methods

a) Synthesis of anionic clay-type materials: bauxite washing tailing from the Amazon were dried at 100 °C for 24 hours, pulverized , homogenized, and labeled as BAUTAI. Subsequently, a 4 g sample was transferred to 100 mL of 30% HCl (v/v) solution and heated (80º C/6 h) to obtain a solution rich in Al^{3+} and Fe^{3+} cations (referred to as SolAlFe). A stoichiometric Mg^{2+}/Al^{3+} ratio of 3:1 was used as the basis for synthesizing 2 g of Mg-based LDH, achieved by adding 4.14 g of $MgCl_2 \cdot 6H_2O$ (Sigma-Aldrich) to 28 mL of the SolAlFe solution under constant stirring for 10 minutes. Subsequently, a NaOH solution (approximately 3.5 $mol \cdot L^{-1}$) was slowly added to the mixture under vigorous stirring at 85 °C for 24 hours, maintaining a pH of approximately 11.2. The final product was filtered, washed with deionized water, dried at room temperature, and designated as MgAlFe. For the synthesis of 2 g of Zn-based LDH, a similar procedure was employed, using a stoichiometric Zn^{2+}/Al^{3+} ratio of 3:1. Approximately 1.9 g of $ZnCl_2$ was added to 19 mL of the SolAlFe solution and stirred vigorously. A NaOH solution (3.5 $mol \cdot L^{-1}$) was then slowly added to the mixture until the pH reached 11. The resulting suspension was subsequently maintained in an oven at 85 °C for 24 hours. The final product was filtered, washed with deionized water, dried at room temperature, and designated as ZnAlFe.

b) Methods of characterization: the chemical composition of the bauxite tailings (BAUTAI) was analyzed using an X-ray fluorescence spectrometer (Axios Minerals, Panalytical). An X-ray diffractometer (XRD) (PANALYTICAL®) was used to carry out the mineral characterization of the raw material and synthetic products under the following test conditions: CoKα radiation source (λ = 1.788920 Å), 30 kV working voltage, 10 mA tube current, and patterns were collected in the range 5–75° 2q with a step size of 0.02° and 0.02 s step length. The structural parameters of the unit cell were obtained following the established methodology for LDH compounds[21], whereas the average crystallite size was derived from XRD peak broadening using the classical Scherrer equation. Raman spectroscopy measurements were conducted at room temperature using a Fourier Transform Raman spectrometer (FT-Raman), model Bruker RF100/S FTR, equipped with a D418-T detector. An Nd:YAG laser with a wavelength of 1064 nm and a power of 150 mW was employed. The spectra were acquired in the spectral range from 40 to 4000 cm^{-1}, with a spectral resolution of 2 cm^{-1}. Infrared transmittance spectra were obtained via attenuated total reflectance Fourier transform infrared spectroscopy (ATR-FTIR) using a Bruker VERTEX 70 model, in the spectral range from 400 to 4000 cm^{-1}, with a spectral resolution of 2 cm^{-1}.

3. Results and Discussion

The chemical composition of BAUTAI was as follows: 31.3 wt% of Al_2O_3, 23.2 wt% of SiO_2, 27.3 wt% of Fe_2O_3, 4.28 wt% of TiO_2, and 13.92 wt% of L.O.I (Loss on ignition). Figure 1a shows X-ray diffraction analysis indicating the mineral phases in BAUTAI. The raw material comprised mainly gibbsite (PDF 00-012-0460), hematite (PDF 00-013-0534), anatase (PDF 01-078-2486), quartz (PDF 01-082-0512) and kaolinite (PDF 00-006-0221), as crystalline phases. It is also possible for amorphous silica and Fe oxyhydroxides to be present[22]. In the ZnAlFe sample (Figure 1b), crystal planes (003), (006), (101), (012), (104), (015), (107), (018), (10 10), (01 11), (110) and (113) were observed at positions 13.5º, 27.2º, 39.52, 40.3º, 43.47, 45.7º, 51.44, 54.72, 62.16, 66.26, 71.11 and 72.11º, respectively. These crystal planes and their respective positions are characteristic of LDH samples, as described in PDF 00-048-1021. Similarly, the XRD patterns of the MgAlFe sample (Figure 1c) showed typical LDH peaks with reflections at 2θ angles of 12.7º, 25.6º, 39.8º, 44.6º, 52.89, 70.65 and 72.12º (PDF 00-024-1110), corresponding to planes (003), (006), (012), (015), (018), (110) and (113), which are close to the positions observed for the ZnAlFe sample. The low intensity of certain peaks in both samples is attributed to the amount of Mg, Zn and Al present in the samples, as discussed in Zhang et al.[23], where an increase in the amount of these elements results in an increase in the intensity of the diffraction peaks. Therefore, both the diffractograms and the crystal planes confirm the anionic clay structures of the samples. Table 1 presents the unit cell parameters and crystallite sizes of the LDH samples synthesized from ZnFeAl–Cl and MgFeAl–Cl. For the ZnFeAl–Cl structure, an interlayer distance of 7.59 Å was observed, along with calculated unit cell parameters of $a = 3.04$ Å and $c = 22.78$ Å, and a crystallite size of 31 nm. These values are in good agreement with those previously reported for ZnFeAl–NO_3 LDHs synthesized from both mining residues (7.62 Å) and commercial reagents (7.54 Å)[24,25], suggesting structural consistency across different interlayer anions, synthetic

Table 1. Interlayer distance (d_{003}), crystal lattice parameters (a and c) and crystallite sizes of the lamellar materials investigated.

LDH structure	Starting material	Basal spacing (Å)		Lattice parameters (Å)		Crystallite size (nm)
		d_{003}	d_{006}	a	c	
ZnFeAl-Cl*	bauxite tailings	7.59	3.80	3.04	22.78	31
MgFeAl-Cl*	bauxite tailings	8.09	4.03	3.08	24.22	46
MgFeAl-NO_3 [24]	saline slag wastes	7.78	3.85	3.08	23.23	~ 8
ZnFeAl-NO_3 [24]	saline slag wastes	7.62	3.82	3.09	22.90	~30
ZnFeAl-NO_3 [25]	commercial reactants	7.54	n.d	3.09	22.63	n.d
MgFeAl-NO_3 [26]	commercial reactants	7.57	n.d	3.03	22.81	21

*Observed in this study. n.d = not determined

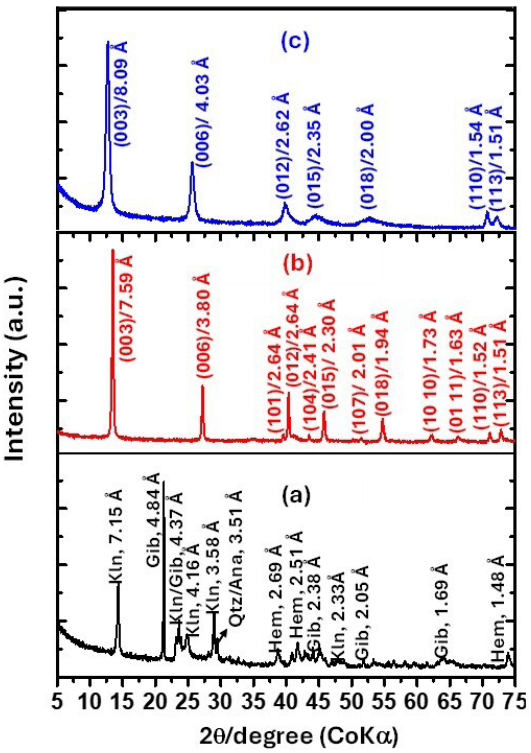

Figure 1. XRD patterns of BAUTAI (a), ZnAlFe (b) and MgAlFe (c) samples. (Kln: kaolinite, Gib: gibbsite; Qtz: quartz; Ana: anatase; Hem: hematite)

approaches, and precursor sources. For the MgFeAl–Cl structure synthesized in this study, an interlayer distance of 8.09 Å was observed, along with unit cell parameters of a = 3.08 Å and c = 24.22 Å, and a crystallite size of 46 nm. These values are slightly higher than those reported for LDHs with the same cationic composition and nitrate as the interlayer anion, synthesized either from mining residues (interlayer distance = 7.78 Å, c = 23.23 Å, crystallite size = 8 nm) or from commercial reagents (interlayer distance = 7.57 Å, c = 20.81 Å, crystallite size = 21 nm)[24,26]. This difference in the observed values may be primarily attributed to the nature of the interlayer anions present in the layered materials.

The morphological and compositional characteristics observed in both MgAlFe and ZnAlFe samples (Figure 2) are in agreement with previously reported studies. For MgAlFe sample (Figure 2a), similar rough surface textures and submicron particle sizes (ranging from 0.1 to 0.3 µm) have been described for Mg-based layered double hydroxides (LDHs), typically attributed to rapid nucleation during synthesis processes[27]. The presence of irregularly shaped, compacted particles in the MgAlFe sample is consistent with the findings of Cui et al.[28] and Golban et al.[29], who reported comparable features in LDHs synthesized under alkaline conditions. On the other hand, the plate-like morphology observed for the ZnAlFe sample (Figure 2b), with particles ranging from 3 to 5 µm, aligns with studies such as Hafez et al.[30], which associate this morphology with the most common layered crystalline structure of based LDHs. The elemental compositions confirmed by EDS (Mg, Al, Fe for MgAlFe; Zn, Al, Fe for ZnAlFe) also match those typically found in ternary LDHs reported in the literature[31-33]. These results reinforce the reproducibility of such structures under similar synthesis conditions and support their potential application in areas such as catalysis and adsorption.

Figure 3 shows the infrared spectra (ATR-FTIR) of the layered double hydroxides in the ternary system, ZnFeAl-Cl (Figure 3a) and MgFeAl-Cl (Figure 3b), while Table 2 lists all the bands observed in this work and in other studies that obtained LDHs from bauxite residues (bauxite washing residues and/or red mud), along with their respective assignments. Initially, both samples exhibited a broad and low-intensity band in the range of 3000 to 3600 cm^{-1}, which is characteristic of O–H stretching vibrations associated with the brucite-like layers of the lamellar materials. Around 1620 cm^{-1}, a narrow band was observed, also attributed to O–H vibrations, but associated with the bending modes of water molecules[16,37-40]. Besides the asymmetric stretching vibration near 1490 cm^{-1} assigned to $M^{2+}M^{3+}$–Cl/CO_3 interactions, bands around 1405 cm^{-1} correspond to high-valence cation–OH (e.g., Ti^{4+}–O–H) stretching in octahedral layers, likely linked to anatase Ti^{4+} in the bauxite residues[36]. In the range between 1370 and 1220 cm^{-1}, bands related to C–O stretching vibrations of carbonate group species (monodentate, bidentate, and bicarbonate) were also identified. The bands near 1365 cm^{-1} in both samples were well correlated with the symmetric stretching of monodentate carbonate groups M–O–CO_2 (M = metal), whereas the band at 1320 cm^{-1} refers to symmetric C–O stretching vibrations of bidentate carbonate groups O–M–O–CO_2. As for the band

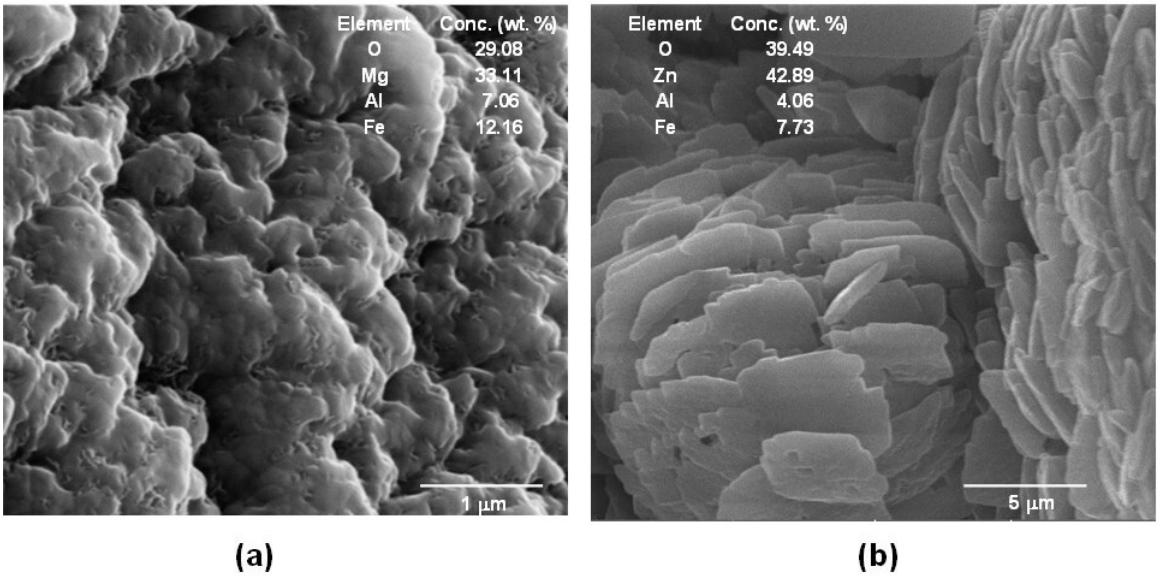

Figure 2. SEM-EDS analyses of MgAlFe (a) and ZnAlFe (b) samples.

Table 2. FTIR band positions of anionic clays synthesized from Bauxite Residues.

Washing bauxite tailings			Red mud			Assignments suggested
ZnFeAl-Cl*	MgFeAl-Cl*	MgFeAl-NO_3 [34]	MgFeAl-Cl [16]	MgAl-CO_3 [35]	CaFeAl-Cl [36]	
3420	3440	3480	3440	3440	3468	O-H groups stretching (brucite-like layers)
1610	1620	1638	1635	1631	1665	O-H bending vibration (water molecules)
1495	1498	-	-	1491	1481	$(M^{2+}+M^{3+})$-(Cl/CO_3) (asymmetric tensile vibration)
1405	1400	-	-	1403	1411	Ti-O-H stretching (brucite-like layers)
1360	1368	1384	-	1361	-	C-O symmetric stretching of monodentate carbonate groups
1312	1318	-	1300	-	-	C-O symmetric stretching of bidentate carbonate groups
1228	1228	-	-	-		C-OH bending mode vibrations of bicarbonate groups
-	984	-	-	-	994	Si-O-Si asymmetric stretching (SiO_3^{2-} anions interlayer space)
870	868	839	-	-		$(M^{2+}+M^{3+})$-OH stretching
775	776	-	785	-	785	$(M^{2+}+M^{3+})$-OH stretching
-	730	-	-	-		$(M^{2+}+M^{3+})$-OH stretching
610	608	-	653	-		M-O-M stretching
-	-	590	-	-	582	$(M^{2+}+M^{3+})$-OH stretching
466	-	400	-	-	424	M-O bending vibration

*Observed in this study. M = Metal

at 1228 cm^{-1}, it was possible to infer that it corresponded to bending mode vibrations of C–OH bonds in bicarbonate groups M–O–CO–OH [40]. Anionic clays, such as layered double hydroxides (LDHs), can adsorb atmospheric CO_2 through molecular interactions at their surface. Following adsorption, CO_2 molecules react with basic sites on the LDH - typically hydroxyl groups - forming carbonate ions (CO_3^{2-}). These carbonate ions are subsequently intercalated into the interlayer galleries of the LDH structure, thereby stabilizing and effectively sequestering the CO_2 within the material. The extent of CO_2 uptake depends on factors like the type of metal ions in the LDH structure, the presence of other intercalated anions, and the specific synthesis conditions[41-43]. It is noteworthy that the band around 984 cm^{-1}, observed in the spectrum of the MgFeAl HDL (Figure 3b), may be attributed to Si–O–Si vibrations of SiO_3^{2-} anionic species located in the interlayer region of the anionic clay[36]. The presence of silicon ions is likely derived from the starting material, similarly to the titanium ions. In the region between 800-400 cm^{-1}, M-O, M-OH and M-O-M type stretching were observed, as evidenced by the band around 870, 775, 610, and 466 cm^{-1}, present in both spectra[37-43].

Figure 4 presents the Raman spectra of the Zn–Fe–Al and Mg–Fe–Al LDH samples, while Table 3 summarizes the Raman bands identified in this study alongside those reported in previous works involving LDHs synthesized from bauxite residues (including bauxite washing residues and red mud). In the Raman spectrum of the MgFeAl sample (Figure 4b), two distinct bands were observed at higher wavenumbers, specifically at 3390 and 3231 cm^{-1}. These bands were attributed to O–H stretching vibrations. The band at 3390 cm^{-1} was associated with O-H stretching region of the M_3OH units (M = Al, Fe

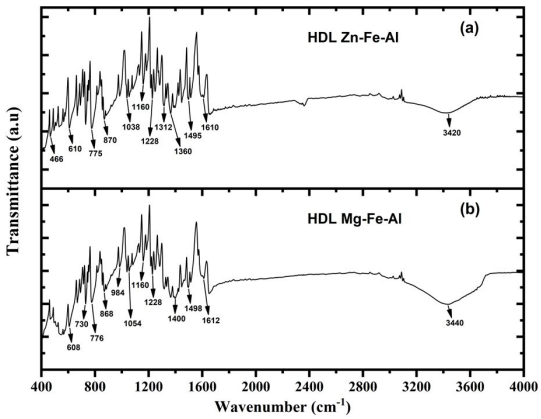

Figure 3. Infrared spectra (a) LDH ZnAlFe and (b) LDH MgAlFe samples.

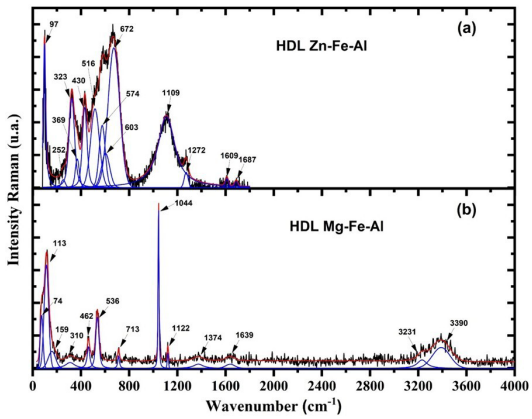

Figure 4. Raman spectra (a) LDH Zn-Fe-Al and (b) LDH Mg-Fe-Al.

Table 3. Raman Band Positions and Vibrational Assignments of Anionic Clays Synthesized from Bauxite Residue.

Washing bauxite tailings			Red mud		Assignments suggested
ZnFeAl-Cl*	MgFeAl-Cl*	MgFeAl-NO_3 [34]	MgFeAl-Cl [44]	MgAl-CO_3 [45]	
-	3390	-	3411	3387	O-H stretching vibrations
-	3231	-	3296	-	O-H stretching vibrations
1272	-	-	-	-	Fe-O stretching
1109	1122	-	-	-	Al-O-H stretching
-	1044	-	1033	1062	C-O stretching (CO_3^{2-} groups)
-	713	711	706	712	Mg-O vibration
672	-	-	679	-	*in-plane* C–O stretching (CO_3^{2-} groups)
603	-	-	-	623	M^{2+}-O-H stretching
574	-	-	560	552	Zn-O-H stretching
-	536	-	542	-	Al-O vibration
516					Fe-O vibration
430	462	466	499	464	M^{2+}-O-H stretching
369	-	-	398	-	Al-O-H stretching
323	310	-	334	303	Fe-O stretching

*Observed in this study. M = Metal

or Mg) within the brucite-like layers. In contrast, the band at 3231 cm^{-1} corresponds to the stretching vibrations of water molecules coordinated to the cations located in the octahedral sheets. These findings suggest the presence of structurally bound water in different chemical environments, indicating successful incorporation of hydroxyl groups and coordinated water into the layered double hydroxide structure. For the band located at 1044 cm^{-1} in the MgFeAl sample (Figure 4b), a correlation was observed with C–O stretching vibrations of carbonate groups associated with Mg_3OH units[45]. In contrast, the band at 672 cm^{-1} in the ZnFeAl sample (Figure 4a) was also associated with carbonate group vibrations but specifically corresponds to in-plane C–O stretching[40]. In the spectrum of the LDH Zn-Fe-Al sample (Figure 4a), low-intensity peaks were observed at 368 and 1109 cm^{-1} whose vibrations were well associated with Al-O-H stretching[46]. In the range between 400 and 600 cm^{-1}, several overlapping bands were observed, forming a broad band of high intensity, with peaks observed at 430 and 603 cm^{-1} which are vibrations associated with M^{2+}-O-H vibrations[47]. The band at 574 cm^{-1} was well associated with Zn–O–H stretching vibrations, indicating the presence of hydroxyl groups coordinated to zinc within the brucite-like layers. Moreover, low intensity bands were observed at 516 and 1272 cm^{-1} corresponding to iron Fe-O vibrations[48]. In the region below 200 cm^{-1}, lattice modes in which the interactions occurring in the crystals were also observed. Three overlapping modes were identified in this region and associated with interactions in the crystal. Additionally, at 536 cm^{-1}, a well-defined low-intensity band was observed and attributed to Al–O vibrations, further confirming the presence of aluminum in the octahedral layers[49,50]. The bands at 310 and 323 cm^{-1} have low intensity and were related to Fe-O stretching[51-53]. At 713 cm^{-1}, a band with very low intensity and barely visible, related to the vibration of Mg-O was identified[49,50]. Some bands observed in Figures 4a and 4b were not identified as vibrations of Mg, Zn, Fe or Al, but were vibrations attributed to LDH[54,55].

4. Conclusions

In this work, the morphology and vibrational properties of ZnAlFe and MgAlFe lamellar double hydroxides (LDHs) were synthesized and investigated. X-ray diffraction (XRD) results confirmed the formation of the characteristic crystalline structure of LDHs and showed that bauxite tailings are viable as precursors in the synthesis of these materials. The differences observed in the intensities of the diffraction peaks indicated that the divalent cations (Zn^{2+} and Mg^{2+}) influenced the crystal structure. Analysis of the chemical composition revealed the presence of metallic oxides, such as Al_2O_3, SiO_2 and Fe_2O_3, from the tailings used. Morphological analysis by scanning electron microscopy (SEM) showed that, despite their similar composition, LDH MgAlFe had a rougher surface, while ZnAlFe formed plate-like agglomerates, indicating that the nature of the divalent cation significantly affected the microstructure of the materials. The spectroscopic analyses (Raman and FT-IR) confirmed the typical interactions of LDHs, as well as the presence of the constituent ions in the synthesized structures. These results show that the substitution of divalent cations allowed the structural and morphological modulation of LDHs, making it possible to modify their physicochemical properties in environmental, catalytic and adsorption applications.

5. References

1. Crepaldi EL, Valim JB. Hidróxidos duplos lamelares: síntese, estrutura, propriedades e aplicações. Quim Nova. 1998;21(3):300-11. http://doi.org/10.1590/S0100-40421998000300011.
2. Wypych F, Freitas RA. Layered double hydroxides and hydroxide salts: structure and properties. In: Wypych F, Freitas RA, editors. Developments in clay science. Amsterdam: Elsevier; 2022. 317 p. (vol. 10).
3. Wang P, Zhang X, Zhou B, Meng F, Wang Y, Wen G. Recent advance of layered double hydroxides materials: Structure, properties, synthesis, modification and applications of wastewater treatment. J Environ Chem Eng. 2023;11(6):111191. http://doi.org/10.1016/j.jece.2023.111191.
4. Kameliya J, Verma A, Dutta P, Arora C, Vyas S, Varma RS. Layered double hydroxide materials: a review on their preparation, characterization, and applications. Inorganics. 2023;11(3):121. http://doi.org/10.3390/inorganics11030121.
5. Chen Y, Zhou S, Li F, Wei J, Dai Y, Chen Y. Fluorescence and phase transitions of Mg-Al-Eu ternary layered double hydroxides – dependence on annealing. Clay Miner. 2011;46(3):487-93. http://doi.org/10.1180/claymin.2011.046.3.487.
6. Yadav DK, Uma S, Nagarajan R. Microwave-assisted synthesis of ternary Li-M-Al LDHs (M = Mg, Co, Ni, Cu, Zn, and Cd) and examining their use in phenol oxidation. Appl Clay Sci. 2022;228:106655. http://doi.org/10.1016/j.clay.2022.106655.
7. Raheem SA, Mohammed AA. Synthesis, characterization, and applications of layered double hydroxides nanocomposites for the adsorption of organic and inorganic contaminants from an aqueous solution: an overview. Results in Surfaces and Interfaces. 2025;18:100386. http://doi.org/10.1016/j.rsurfi.2024.100386.
8. Willems E, van Velthoven N, Smolders E, Everaert M. One-pot synthesis of MgAl layered double hydroxides (LDH) from weathered tropical soils. Appl Clay Sci. 2024;261:107580. http://doi.org/10.1016/j.clay.2024.107580.
9. Hosni K, Srasra E. Simplified synthesis of layered double hydroxide using a natural source of magnesium. Appl Clay Sci. 2009;43(3-4):415-9. http://doi.org/10.1016/j.clay.2008.12.008.
10. Wajima T. Synthesis of Fe-layered double hydroxide from bittern and its nitrate-ion removal ability. Clay Miner. 2021;56(1):65-74. http://doi.org/10.1180/clm.2021.17.
11. Jafari Foruzin L, Rezvani Z, Habibi B. New ternary-component layered double hydroxide as a low-cost and efficient electrocatalyst for water oxidation: NiCaFe-LDH from eggshell bio-waste. Appl Clay Sci. 2020;188:105511. http://doi.org/10.1016/j.clay.2020.105511.
12. Wang Q, Peng Y, Chen M, Xu M, Ding J, Yao Q, et al. Synthesis of layered double hydroxides from municipal solid waste incineration fly ash for heavy metal adsorption. Sci Total Environ. 2024;912:169482. http://doi.org/10.1016/j.scitotenv.2023.169482.
13. Boulahbal AI, Santamaría L, Azizi A, Boutahala M, Korili SA, Gil A. Synthesis of Cu-Al layered double hydroxides from aluminum saline slags. Miner Eng. 2023;204:108413. http://doi.org/10.1016/j.mineng.2023.108413.
14. Li T, Wang Q, He Y, Ma J, Wang X, Bai J, et al. Preparation of CaMgAl hydrotalcite from electrode aluminum-foil industrial wastewater for high-temperature CO_2 capture. Chem Eng J. 2025;505:159242. http://doi.org/10.1016/j.cej.2025.159242.
15. Wu H, Zhang W, Zhang H, Gao P, Jin L, Pan Y, et al. Synthesis of layered double hydroxides with phosphate tailings and its effect on flame retardancy of epoxy resin. Polymers. 2022;14(13):2516. http://doi.org/10.3390/polym14132516.
16. Cunha MVPO, Corrêa JAM. Synthesis and characterization of layered double hydroxides from red mud. Ceramica. 2011;57(341):85-93. http://doi.org/10.1590/S0366-69132011000100011.

17. Kloprogge JT, Hickey L, Frost RL. FT-Raman and FT-IR spectroscopic study of synthetic Mg/Zn/Al-hydrotalcites. J Raman Spectrosc. 2004;35(11):967-74. http://doi.org/10.1002/jrs.1244.
18. Frost RL, Erickson KL. Raman spectroscopic study of the hydrotalcite desautelsite $Mg_6Mn_2CO_3(OH)_{16}.4H_2O$. Spectrochim Acta A Mol Biomol Spectrosc. 2005;61(11-12):2697-701. http://doi.org/10.1016/j.saa.2004.10.012.
19. Frost RL, Weier MT, Kloprogge JT. Raman spectroscopy of some natural hydrotalcites with sulphate and carbonate in the interlayer. J Raman Spectrosc. 2003;34(10):760-8. http://doi.org/10.1002/jrs.1050.
20. Frost RL, Musumeci AW, Kloprogge JT, Adebajo MO, Martens WN. Raman spectroscopy of hydrotalcites with phosphate in the interlayer: implications for the removal of phosphate from water. J Raman Spectrosc. 2006;37(7):733-41. http://doi.org/10.1002/jrs.1500.
21. Parida K, Mohapatra L, Baliarsingh N. Effect of Co^{2+} substitution in the framework of carbonate intercalated Cu/Cr LDH on structural, electronic, optical, and photocatalytic properties. J Phys Chem C. 2012;116(42):22417-24. http://doi.org/10.1021/jp307353f.
22. Negrão LBA, Costa ML, Pöllmann H. The Belterra Clay on the bauxite deposits of Rondon do Pará, Eastern Amazon. Braz J Geol. 2018;48(3):473-84. http://doi.org/10.1590/2317-4889201820180128.
23. Zhang J, Wang X, Ma L, Yu X, Ma Q, Fan S, et al. Preparation of layered K/Mg-Fe-Al catalysts and its catalytic performances in CO hydrogenation. J Fuel Chem Technol. 2017;45(12):1489-98. http://doi.org/10.1016/S1872-5813(17)30066-X.
24. Santamaría L, Oliveira García L, Faria EH, Ciuffi KJ, Vicente MA, Korili SA, et al. (II)-Al-Fe layered double hydroxides synthesized from aluminum saline slag wastes and catalytic performance on cyclooctene oxidation. Miner Eng. 2022;180:107516. http://doi.org/10.1016/j.mineng.2022.107516.
25. Pastor A, Rodriguez-Rivas F, Miguel G, Cruz-Yusta M, Martin F, Pavlovic I, et al. Effects of Fe^{3+} substitution on Zn-Al layered double hydroxides for enhanced NO photochemical abatement. Chem Eng J. 2020;387:124110. http://doi.org/10.1016/j.cej.2020.124110.
26. Naseem S, Gevers B, Boldt R, Labuschagné FJWJ, Leuteritz A. Comparison of transition metal (Fe, Co, Ni, Cu, and Zn) containing tri-metal layered double hydroxides (LDHs) prepared by urea hydrolysis. RSC Advances. 2019;9(6):3030-40. http://doi.org/10.1039/C8RA10165E.
27. Velázquez-Herrera FD, Zarazua-Aguilar Y, Garzón-Pérez AS, Álvarez-Gómez KM, Fetter G. Composites formed by layered double hydroxides with inorganic compounds: an overview of the synthesis methods and characteristics. MethodsX. 2024;13:102912. http://doi.org/10.1016/j.mex.2024.102912.
28. Cui C, Zhang L, Xie F, Zhu C, Yu B. Ternary MgAlFe-layered double hydroxide: synthesis, characterization, and application in photocatalytic degradation. ChemistrySelect. 2024;9(43):e202403096. http://doi.org/10.1002/slct.202403096.
29. Golban A, Lupa L, Cocheci L, Pode R. Synthesis of MgFe layered double hydroxide from iron-containing acidic residual solution and its adsorption performance. Crystals. 2019;9(10):514. http://doi.org/10.3390/cryst9100514.
30. Hafez MAH, Kenawy IMM, Abd Elbary ZME, Elmorsi RR, Abou-El-Sherbini KS. Removal of Cr(VI) from aqueous media on calcined (Mg-Zn)/(Al-Fe)-(CO_3)/Cl layered double hydroxides. Desalination Water Treat. 2019;148:270-84. http://doi.org/10.5004/dwt.2019.23742.
31. Luengo CV, Lopez NA, Ramos CP, Avena MJ. Highly efficient arsenic adsorption onto Mg/Al/Fe layered double hydroxides: kinetics, isotherm, XPS and Mössbauer spectroscopies. J Water Process Eng. 2023;56:104542. http://doi.org/10.1016/j.jwpe.2023.104542.
32. Valente JS, Hernandez-Cortez J, Cantu MS, Ferrat G, López-Salinas G. Calcined layered double hydroxides Mg–Me–Al (Me: Cu, Fe, Ni, Zn) as bifunctional catalysts. Catal Today. 2010;150(3-4):340-5. http://doi.org/10.1016/j.cattod.2009.08.020.
33. Crespo I, Barriga C, Ulibarri MA, González-Bandera G, Malet P, Rives V. An X-ray diffraction and absorption study of the phases formed upon calcination of Zn−Al−Fe hydrotalcites. Chem Mater. 2001;13(5):1518-27. http://doi.org/10.1021/cm0010856.
34. Nascimento RS, Correa JAM, Figueira BAM, Pinheiro PA, Silva JH, Freire PTC, et al. From mining waste to environmetal remediation: a nanoadsorbent from Amazon bauxite tailings for the removal of erythrosine B dye. Appl Clay Sci. 2022;222:106482. http://doi.org/10.1016/j.clay.2022.106482.
35. Palmer SJ, Frost RL. Characterization of Bayer hydrotalcites formed from bauxite refinery residue liquor. Ind Eng Chem Res. 2011;50(9):5346-51. http://doi.org/10.1021/ie1018194.
36. Tang L, Wang L, Qin H, Wang X. Application of red mud acid activation treatment leaching solution for preparation of functionalized layered double hydroxides. Mater Chem Phys. 2025;341:130950. http://doi.org/10.1016/j.matchemphys.2025.130950.
37. Ghemit R, Boutahala M, Kahoul A. Removal of diclofenac from water with calcined ZnAlFe-CO3 layered double hydroxides: effect of contact time, concentration, pH and temperature, Desalin. Desalination Water Treat. 2017;83:75-85. http://doi.org/10.5004/dwt.2017.21031.
38. Chu L, Zhang C, Yu J, Sun X, Zhou X, Zhang Y. Adsorption of nitrate from interflow by the Mg/Fe calcined layered double hydroxides. Water Sci Technol. 2022;86(3):511-29. http://doi.org/10.2166/wst.2022.224.
39. Sajid M, Ihsanullah I. Magnetic layered double hydroxide-based composites as sustainable adsorbent materials for water treatment applications: progress, challenges, and outlook. Sci Total Environ. 2023;880:163299. http://doi.org/10.1016/j.scitotenv.2023.163299.
40. Palmer SJ. Stability of hydrotalcites formed from Bayer refinery environmental control processes [thesis]. Brisbane: Queensland University of Technology; 2010.
41. Tan XY, Ungur L, Chin WS. Carbonate-free CoAl layered double hydroxides supercapacitors: controlled precipitation via acid mediated decomplexation. Appl Clay Sci. 2022;224:106519. http://doi.org/10.1016/j.clay.2022.106519.
42. Shanmuganathan K, Ellison CJ. Layered double hydroxides: an emerging class of flame retardants. In: Papaspyrides CD, Kiliaris P, editors. Polymer green flame retardants. Amsterdam: Elsevier; 2014. Chapter 20, p. 675-707. http://doi.org/10.1016/B978-0-444-53808-6.00020-2.
43. Zhang S, Lee J, Li B, Zhang T, Baeck S-H, Shim SE. Industrial solid waste-based layered double hydroxide composite with enhanced adsorption affinity to Congo red, acid red, and reactive red. Korean J Chem Eng. 2024;41(3):829-38. http://doi.org/10.1007/s11814-024-00088-3.
44. Cunha MVP. Síntese e caracterização de hidróxidos duplos lamelares a partir da lama vermelha [tese]. Belém: Universidade Federal do Pará; 2011.
45. Frost RL, Reddy BJ. Thermo-Raman spectroscopic study of the natural layered double hydroxide manasseite. Spectrochim Acta A Mol Biomol Spectrosc. 2006;65(3-4):553-9. http://doi.org/10.1016/j.saa.2005.12.007.
46. Demirok G, Atilgan S, Li H. Raman spectroscopic study and statistical modeling of composition-structure-property of MgO-CaO-Al2O_3-SiO_2 based glasses. J Non-Cryst Solids. 2024;626:122787. http://doi.org/10.1016/j.jnoncrysol.2023.122787.
47. Bhapkar AR, Geetha M, Jaspal D, Gheisari K, Laad M, Cabibihan J-J, et al. Aluminium doped ZnO nanostructures for efficient photodegradation of indigo carmine and azo carmine G in solar irradiation. Appl Nanosci. 2023;13(8):5777-93. http://doi.org/10.1007/s13204-023-02824-3.
48. Thyr J, Österlund L, Edvinsson T. Polarized and non-polarized Raman spectroscopy of ZnO crystals: method for determination of crystal growth and crystal plane orientation for nanomaterials. J Raman Spectrosc. 2021;52(8):1395-405. http://doi.org/10.1002/jrs.6148.

49. Biswal S, Bhaskaram DS, Govindaraj G. Role of graphene oxide in modifying magnetism in α-Fe_2O_3 nanoparticles: raman and magnetization studies. Mater Chem Phys. 2021;266:124531. http://doi.org/10.1016/j.matchemphys.2021.124531.
50. Liu Y, Cheng B, Wang K-K, Ling G-P, Cai J, Song C-L, et al. Study of Raman spectra for γ-Al_2O_3 models by using first-principles method. Solid State Commun. 2014;178:16-22. http://doi.org/10.1016/j.ssc.2013.09.030.
51. Ghule AV, Ghule K, Punde T, Liu J-Y, Tzing S-H, Chang J-Y, et al. In situ monitoring of NiO–Al_2O_3 nanoparticles synthesis by thermo-Raman spectroscopy. Mater Chem Phys. 2010;119(1-2):86-92. http://doi.org/10.1016/j.matchemphys.2009.07.050.
52. Mo R, Liu Q, Li H, Yang S, Zhong J. Photoelectrochemical water oxidation in α-Fe_2O_3 thin films enhanced by a controllable wet-chemical Ti-doping strategy and Co–Pi co-catalyst modification. J Mater Sci Mater Electron. 2019;30(24):21444-53. http://doi.org/10.1007/s10854-019-02525-0.
53. Daoudi K, El-Helali S, Othmen Z, Suleiman BM, Tsuchiya T. Microstructure and electrical transport mechanisms of the Ca-doped LaMnO3 films grown on MgO substrate. J Mater. 2020;6(1):17-23. http://doi.org/10.1016/j.jmat.2019.10.002.
54. Kloprogge JT, Frost RL. Infrared and Raman spectroscopic studies of layered double hydroxides (LDHs). In: Rives V, editor. Layered double hydroxides: present and future. New York: Nova Science Publishers; 2001. p. 139-92. Chapter 5.
55. Kloprogge JT, Frost RL. Fourier transform infrared and Raman spectroscopic study of the local structure of Mg-, Ni-, and Co-hydrotalcites. J Solid State Chem. 1999;146(2):506-15. http://doi.org/10.1006/jssc.1999.8413.

Data Availability

Data are available on reasonable request to the corresponding author.